How a raindrop gets shattered on biological surfaces

Seungho Kim[a], Zixuan Wu[a], Ehsan Esmaili[a], Jason J. Dombroskie[b], and Sunghwan Jung[a,1]

[a]Department of Biological and Environmental Engineering, Cornell University, Ithaca, NY 14853; and [b]Department of Entomology, Cornell University, Ithaca, NY 14853

Edited by Joanna Aizenberg, Harvard University, Cambridge, MA, and approved May 14, 2020 (received for review February 15, 2020)

Many biological surfaces of animals and plants (e.g., bird feathers, insect wings, plant leaves, etc.) are superhydrophobic with rough surfaces at different length scales. Previous studies have focused on a simple drop-bouncing behavior on biological surfaces with low-speed impacts. However, we observed that an impacting drop at high speeds exhibits more complicated dynamics with unexpected shock-like patterns: Hundreds of shock-like waves are formed on the spreading drop, and the drop is then abruptly fragmented along with multiple nucleating holes. Such drop dynamics result in the rapid retraction of the spreading drop and thereby a more than twofold decrease in contact time. Our results may shed light on potential biological advantages of hypothermia risk reduction for endothermic animals and spore spreading enhancement for fungi via wave-induced drop fragmentation.

drop impact | microstructures | superhydrophobic surfaces | contact time

Superhydrophobic structures at the nanoscale are known to prevent the penetration of the liquid toward the nanostructures (1). However, structures at the microscale cause a liquid-pinning behavior by allowing the liquid to penetrate into the gaps between the microstructures (2), thereby leading to the increase in the residence/contact time of a bouncing drop on a solid (3). As a result, mass, momentum, and heat transfers are enhanced between the drop and the substrate (4–6), while hindering other known functions such as self-cleaning (7), anti-icing (8), antifogging (9), and robust superhydrophobicity (10). Therefore, nanostructures have been considered to be more valuable to achieve such prominent superhydrophobic functionalities, compared to microstructures.

Recently, drop impact on engineered microscale structures has been known to exhibit asymmetric spreading (11) and retraction (4) and a pancake-shaped rebouncing (12), finally leading to the rapid drop detachment with a significant decrease in the contact time (4, 12). However, the role of microscale structures during drop impact was underestimated since most studies have focused on drop impacts at low speeds (4, 5, 13, 14), much lower than real raindrop impact speeds in natural events.

In this present study, we demonstrate that an impacting drop at high speeds can generate shock-like surface waves in the presence of surface morphology at the microscale. The top air–liquid interface of the spreading liquid is perturbed due to the shock waves and becomes vulnerable to film ruptures via hole nucleation. Finally, the holes grow in time and coalesce with each other. As a result, the contact time is reduced about 70%, and, correspondingly, the heat and momentum transfers of the impacting drop onto the substrate are reduced (5). Therefore, our findings may elucidate functional benefits in terms of hypothermia risk, flight stability, and spore dispersal of biological surfaces triggered by the microscale structures.

Results

Experiments. We prepared various biological specimens including bird feathers, insects, and plant leaves (*Materials and Methods*). Then, a water drop is released to impact these biological surfaces. Here, the drop radius, R, and the impact velocity, U range from 1.1 to 2.0 mm and 0.7 to 6.6 m/s, respectively. The corresponding Weber number, $\mathrm{We}=\rho U^2(2R)/\gamma$, ranges from 15 to 2,000, which covers the typical We of rainfall (15, 16). Here, ρ and γ are the density ($=1{,}000\ \mathrm{kg/m^3}$) and the surface tension ($=72$ mN/m), respectively. The dynamics of drop impact were captured by a high-speed camera at a frame rate of $5{,}000$ to $20{,}000\ \mathrm{s^{-1}}$ with a resolution of $1{,}024 \times 672$ pixels. Selected drop motions on these biological surfaces are illustrated in Fig. 1.

Drop Impact on Biological Surfaces. Fig. 1*A* shows a drop impact on a bird feather, whose surface is superhydrophobic with surface roughness at different scales (17). Fig. 1*A*, *Center Left Inset* shows the hierarchical structure: Microscale barbules emerge from barbs attached to a millimeter-scale rachis. When a drop impacts the feather at a high speed ($\mathrm{We} \approx 1{,}000$), the liquid–air interface of the spreading drop is disturbed and generates hundreds of V-shaped, shock-like waves, as shown in Fig. 1*A*, *Center Inset*. A typical shock wave is observed when a compressible fluid experiences density discontinuity and forms a V-shaped wave pattern. In our case, the wave observed is not a classic shock wave since the fluid is incompressible at speeds in our experiments and exhibits uniform density. However, similar V-shaped waves result from discontinuity in film thickness of the spreading drop instead of density variations (Fig. 1, *Center Insets*). Therefore, even though the fluid is not compressed, we term the wave pattern "shock-like waves" in this present work. Similar shock-like waves have been observed as a wake structure on a liquid curtain behind an external perturbation (18) or an oblique liquid flow in a soap film (19). Then, the spreading drop is abruptly shattered/fragmented (Fig. 1*A*, *Right*) shortly after rupturing the liquid film and nucleating holes (Fig. 1*A*, *Center Right*). A similar morphological transition of an impacting drop was also observed

Significance

Rainfall on biological superhydrophobic surfaces is ubiquitous in nature. Previous studies in a laboratory setting have focused only on low-speed impacts, which can be quite different from rain conditions in nature. In this study, we reported unexpected and interesting shock-like patterns when a drop impacts biological surfaces at high speeds. These shock-like waves trigger sudden drop fragmentation into smaller satellite droplets and lead to a more than twofold decrease in contact time. Our findings may elucidate biological advantages (hypothermia risk reduction for birds, flight stability for insects, spore dispersal on plants) of superhydrophobic surfaces triggered by microstructures.

Author contributions: S.K., E.E., J.J.D., and S.J. designed research; S.K., Z.W., and S.J. performed research; S.K., Z.W., and S.J. analyzed data; S.K., Z.W., and S.J. wrote the paper; and E.E. prepared micropatterned surfaces.

The authors declare no competing interest.

This article is a PNAS Direct Submission.

Data deposition: The data reported in this paper have been deposited in the Open Science Framework (OSF) database, DOI 10.17605/OSF.IO/6RD8K.

See online for related content such as Commentaries.

[1]To whom correspondence may be addressed. Email: sunnyjsh@cornell.edu.

This article contains supporting information online at https://www.pnas.org/lookup/suppl/doi:10.1073/pnas.2002924117/-/DCSupplemental.

First published June 8, 2020.

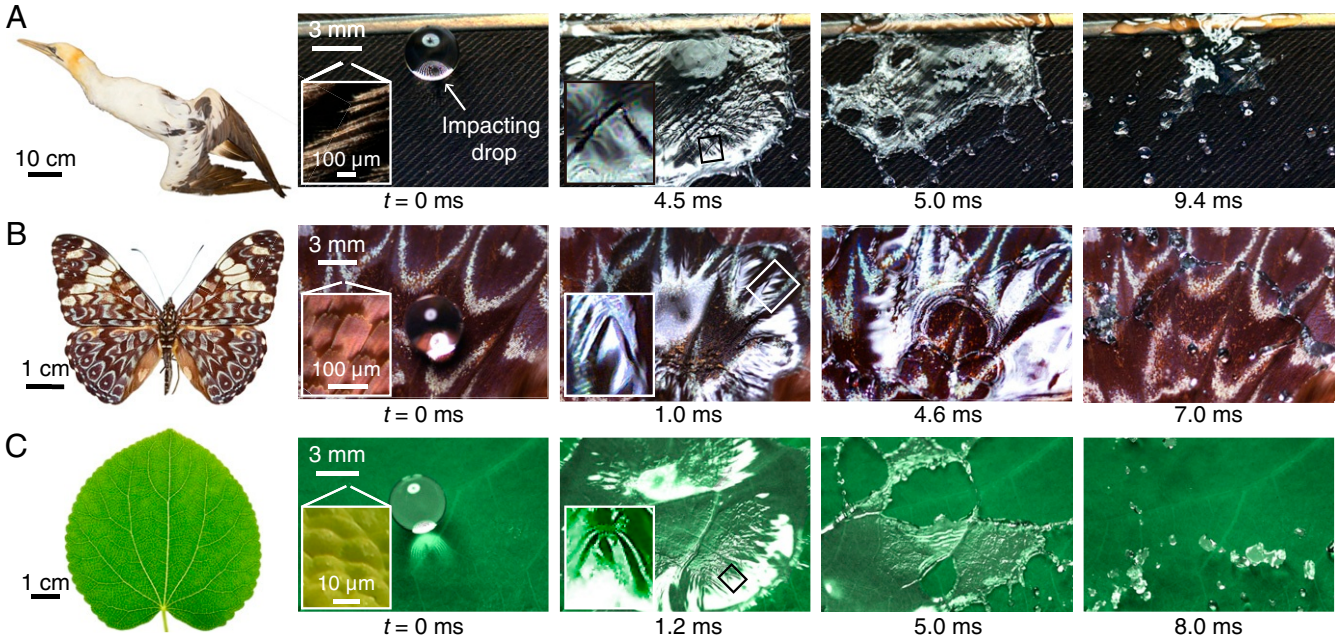

Fig. 1. (*A–C*) Biological surfaces for drop impact experiments (*Left*) and sequential events after the impact of a water drop of 1.7 mm in radius on the biological surfaces (from *Left* to *Right*). (*A*) Northern gannet feather, where [*U*, We] = [4.6 ms^{-1}, 970]. (*B*) Cracker butterfly wing, where [*U*, We] = [4.2 ms^{-1}, 810]. (*C*) Katsura leaf, where [*U*, We] = [5.4 ms^{-1}, 1,340]. *A–C*, *Center Left Insets* represent the microscopic images of each biological surface achieved by a focus-stacking technique. *A–C*, *Center Insets* visualize shock waves on a spreading drop in the presence of physical morphology at the microscale. The spreading drop is suddenly ruptured by nucleating multiple holes (*Center Right*). Finally, the holes grow and coalesce with each other, thereby breaking into smaller satellite droplets (*Right*). Corresponding videos are included in Movie S1.

for other biological surfaces such as insect wings and plant leaves as in Fig. 1 *B* and *C* (Movies S2 and S3). All these specimens have hierarchical superhydrophobic structures, where an array of micrometer-sized bumps exists with nanoscale structures (20, 21).

Drop Impact on Artificial Surfaces. To further investigate details of the shock-like wave structure, we prepared two types of substrate with different wettability. One is a hydrophilic glass surface, and the other is a superhydrophobic surface coated by hierarchical micro- and nanostructures (*Materials and Methods*). On the smooth hydrophilic substrate, a drop merely spreads by forming a radially expanding rim as in Fig. 2*A*. On the superhydrophobic glass, a drop spreads, retracts, and bounces at a low-impact speed (Fig. 2*B*), whereas a drop with a high-impact speed exhibits shock-like surface waves and destructive breakup dynamics as in Fig. 2*C*.

At a high U, hundreds of shock-like surface waves were generated in the presence of microscale bumpy structures as in Fig. 2*C*, *Center Left*. A drop spreads and then is suddenly ruptured, as holes are nucleated (Fig. 2*C*, *Center*). Eventually, the spreading drop is shattered into smaller satellite droplets (Fig. 2*C*, *Right*) as the holes get bigger and coalesce. Similar dynamics were observed on a micropatterned surface (type III) with constant spacing and height of bumps as in Fig. 2*D*. Therefore, we confirmed that, when a drop impacts hierarchical superhydrophobic surfaces with a high-impact velocity, microscale bumpy structures can perturb the spreading drop to generate the numerous shock-like waves on the liquid–air interface and eventually break into smaller droplets.

Such spreading and fragmentation behaviors greatly lower the residence/contact time of a drop on a solid substrate. For a typical bouncing drop (Fig. 2*B*) with low-impact velocities, the measured contact time (≃18 ms) almost follows the theoretical capillary contact time, 19 ms, estimated from $\tau = 2.3\sqrt{\rho R^3/\gamma}$ (6). However, the shock-induced drop fragmentation leads to a more than twofold decrease in the contact time compared to the theoretical expectation as shown in Fig. 2.

Shape of Shock-Like Waves. Fig. 3*A* shows the schematic of how a shock-like wave is generated above a microbump on the surface as a drop spreads. Experimentally, we confirmed that the half angle of the shock-like wave increases with an elapsed time (Fig. 3*B*, *Insets*) and decreases with the radial distance from the center to a bump r_b. Fig. 3*C* clearly shows the dependency of ψ on t and r_b for various hierarchical superhydrophobic surfaces.

In analogy to the Mach shock wave, the half angle of the shock-like wave, ψ, might be determined by the distance ratio of $u_w\, t$ to $u\, t$; $\sin\psi = u_w/u = 1/\mathrm{Ma}^*$. Here, u_w is the speed of wave propagation, u is the fluid velocity (18, 19), and Ma is the equivalent Mach number as $\mathrm{Ma}^* = u/u_w$.

Here, u can be approximated by r/t with r being the radial distance from the drop center. This model for u was suggested in the case of a spreading liquid sheet in the air after the drop impact on a small target object, a so-called drop-impact version of the Savart sheet (22–24). Although a drop spreads on a solid substrate in our case, we confirmed that the relation $u \approx r/t$ is in good agreement with experiments due to negligible viscous stress on a superhydrophobic substrate (model validation in *SI Appendix*, section A). For the wave propagation speed, u_w, we assumed that the wave propagates under the capillary action, leading to $u_w = \sqrt{2\gamma/(\rho h)}$, where γ and h are the surface tension and the film thickness of a spreading drop, respectively (18, 19, 25). Hence, we express ψ as

$$\sin\psi = \frac{1}{\mathrm{Ma}^*} = \frac{\sqrt{2\gamma/(\rho h)}}{r/t}. \qquad [1]$$

Here, the film thickness, $h(r,t)$, can be approximated as $R^3/(U^2t^2)(Ut/r)^n$, where $n = 3$ in the early stage (23, 25), 2 in

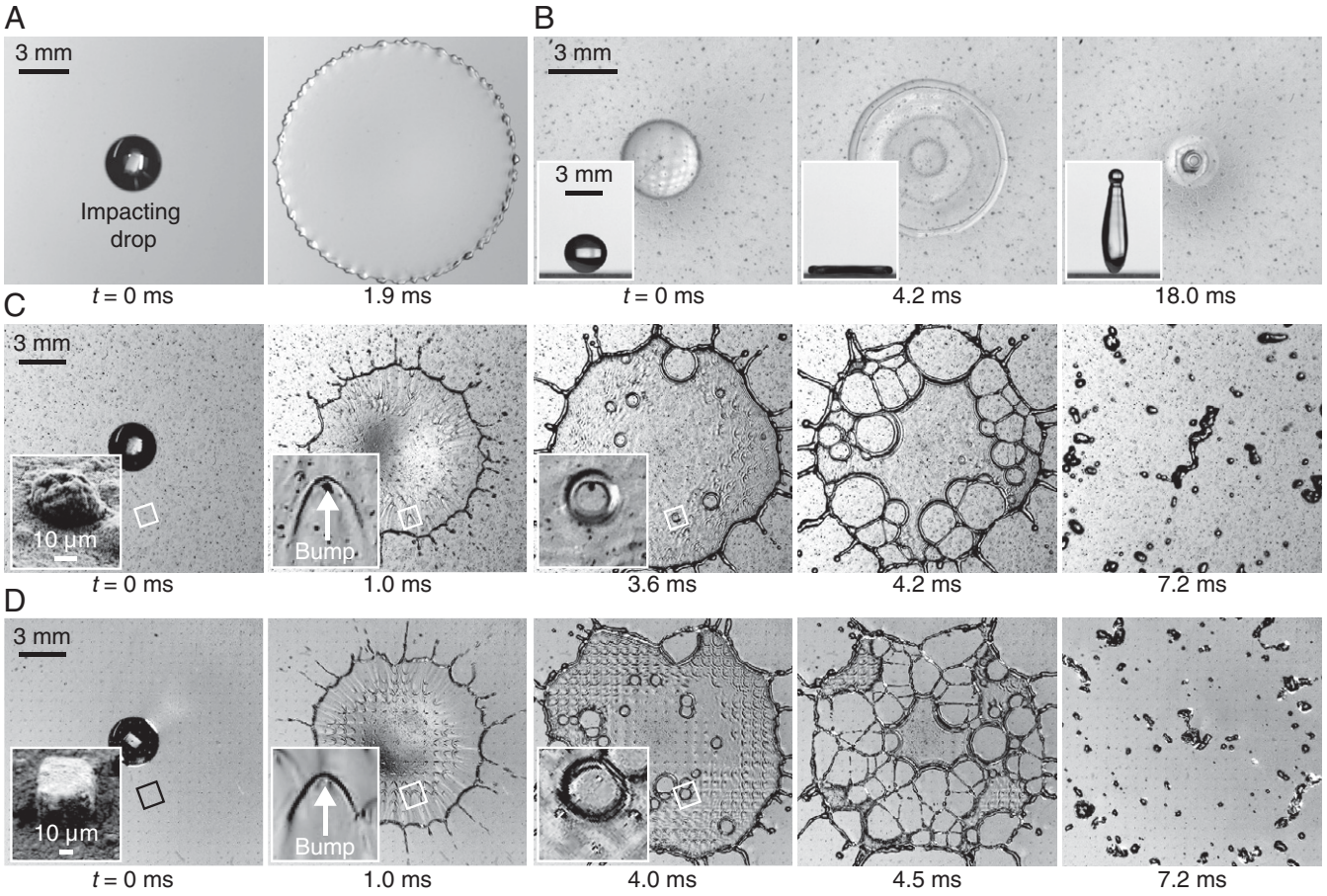

Fig. 2. Bottom-view images of an impacting drop with 1.7 mm in radius on artificial surfaces. (*A*) Drop impact on a smooth glass for high-impact velocity, where [*U*, We] are [3.8 m/s, 680]. (*B* and *C*) Drop impact on a glass coated by hierarchical superhydrophobic structures (type I) for low-impact velocity (*B*) and for high-impact velocity (*C*). Corresponding [*U*, We] are [0.9 m/s, 40], [3.8 m/s, 680], respectively. *Insets* in *B* represent the side-view image of drop impact achieved by a synchronized high-speed camera. *Insets* in *C* are magnified images of the local area to clearly show the microbump, the shock-like wave on the microbump, and the nucleated hole followed by the shock-like wave, respectively. For low *U*, the impacting drop merely spreads, retracts, and rebounds, whereas for high *U*, hundreds of shock-like waves are generated on the spreading drop (*Center Left*), and then a number of holes are abruptly nucleated (*Center*), which grow in time simultaneously (*Center Right*). Finally, the contact time between the drop and the substrate gets shortened by breaking into smaller satellite droplets (*Right*). (*D*) Similar dynamics were observed on a different superhydrophobic surface with regularly spaced microbumps (type III), where [*U*, We] are [3.8 m/s, 680]. The corresponding videos are in Movies S4 and S5, respectively.

the middle stage (23, 24), and 0 in the late stage of a spreading drop (validation in *SI Appendix*, section B). Based on Eq. **1** along with this film-thickness model, the scattered data in Fig. 3*C* are collapsed onto a single line in Fig. 3*D*.

Hole Nucleation Criterion. Above a critical impact velocity, U_c, a number of shock-like waves form and interfere with each other. As a result, the shock-like waves create the nonuniform film thickness of a spreading drop with a certain amplitude, $|\eta|$, as depicted in Fig. 4*A*, thereby leading to a wrinkled pattern on the spreading drop. Then, we observed the sudden formation of holes/ruptures at the same locations where the shock-like waves are formed during the drop-receding stage (Fig. 2 *C* and *D*, *Center*). For this later drop-receding stage, the film thickness is independent of the radial position; $h(t) \sim R^3/(Ut)^2$, as delineated above. This shock-like wave decreases and propagates upstream toward the drop center (Fig. 4*A* and *SI Appendix*, section C) since $u_w \gg u$ at the drop-receding stage. Then, the liquid film is ruptured as the trough of the perturbed film touches the top of a microbump (Fig. 4*A*, *Right*). This scenario suggests the following threshold criterion, $h(t) - |\eta| \approx \epsilon$, with ϵ being the height of the microbump. Fig. 2 *C* and *D* shows that the rupturing hole is nucleated on top of the bump apex, which validates our assumption.

Hole Nucleation Timescale. Now, we estimate the hole nucleation time, t_{hole}, defined as the time interval between when a drop impacts and when the first hole is formed. Fig. 4*B* shows that t_{hole} decreases with the impact velocity, U. Here, we consider two limit cases. First, the impact velocity is well above the critical velocity ($U \gg U_c$), and holes are nucleated on a spreading drop when the drop-spreading radius is close to its maximum radius (Fig. 2 *C* and *D*). In this case, the spreading drop is observed to have highly wrinkled patterns, indicating that the amplitude of the perturbed interface, $|\eta|$, is large enough to play a significant role in rupturing the film. To estimate the undulation amplitude, we used the unsteady Bernoulli equation to get the dispersion relation of shock-like waves; $|\eta| = \alpha\epsilon u\sqrt{\rho/(\gamma k)}$, where α and k represent a constant coefficient and wavenumber, respectively (see *SI Appendix*, section D in detail). Then, by using $t_{\mathrm{spread}}(\approx 16R/(3U))$ (26) for the characteristic timescale of $|\eta|$ and imposing a geometric threshold condition for the hole nucleation ($h(t) - |\eta| \approx \epsilon$), we obtain the asymptotic solution for t_{hole} as

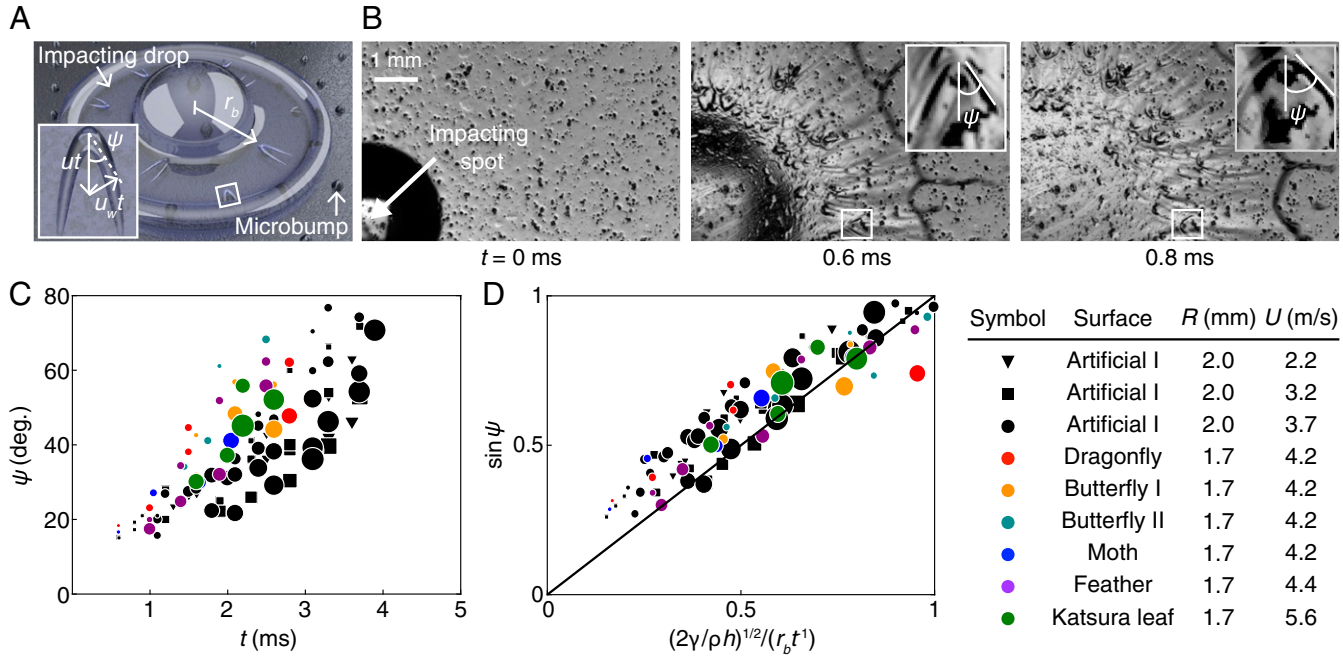

Fig. 3. (*A*) Schematic of the formation of shock-like waves by microbumps, where r_b, u, u_w, and ψ represent the radial distance of the microbump measured from the drop center, the flow velocity of the spreading drop, the speed of wave propagation, and the half angle of the shock wave, respectively. (*B*) Sequential images of the shape changes of shock waves after the drop of 1.7 mm in radius impacts an artificial superhydrophobic surface (type I) at $U = 4.2$ m/s (We = 826). *Insets* show the magnified view of the shock-like wave. (*C*) Experimentally measured ψ versus t, where the size of symbols is proportional to the microbump location, r_b. Hence, the larger symbols mean the farther distance from the center. (*D*) Half angle, ψ, plotted vs. the theoretical expectation based on Eq. **1**.

$$t_{\rm hole} \simeq \left[1 + a\sqrt{\frac{\rho}{\gamma k}}\right]^{-1/2} \epsilon^{-1/2} R^{3/2} U^{-1} \quad \text{for } U \gg U_c, \qquad [2]$$

where $a = (3\alpha/16)\, U{\rm We}^{1/4}$.

Second, when $U \approx U_c$, a single hole appears just before the drop rebounds (Movie S6). Thus, the hole formation time, $t_{\rm hole}$, gets close to the capillary contact time, $\tau = 2.3\sqrt{\rho R^3/\gamma}$ (6). In this limit case, a shock-like wave on a microbump has a small amplitude and is dissipated quickly to become quite a smooth interface. By assuming $|\eta| \approx 0$ (i.e., $\alpha \approx 0$) in Eq. **2**, we get the upper limit of $t_{\rm hole}$ as

$$t_{\rm hole} \simeq \epsilon^{-1/2} R^{3/2} U^{-1} \quad \text{for } U \approx U_c. \qquad [3]$$

The dispersed data of $t_{\rm hole}$ in Fig. 4*B* are collapsed between the two theoretical limits (Eqs. **2** and **3**) as shown in Fig. 4*C*. Here, the upper and lower dashed lines for Eq. **2** are from variations in k values in biological samples (Table 1): The lower and upper limits are based on butterfly I and feathers, respectively.

Finally, we can determine the critical impact velocity, U_c. At $U \approx U_c$, a spreading drop starts having a hole formed just before the drop bounces off. It indicates that the hole formation time in Eq. **3** equals to the capillary contact time, τ. Then, we obtained an expression of the threshold impact velocity as

$$U_c \sim \sqrt{\frac{\gamma}{\rho\epsilon}}. \qquad [4]$$

The experimental data in Fig. 4*D* are well collapsed onto the single line in Fig. 4*E* based on our theoretical model, Eq. **4**. Also, it is worth noting that this model predicts the independence of U_c on R (see *SI Appendix*, section E in detail).

Drop Fragmentation. For $U > U_c$, once holes are nucleated on a spreading drop, the holes rapidly expand to lower its surface energy over hydrophobic nanostructured surfaces. On superhydrophobic surfaces, the holes expand at a speed of $v_h \approx \sqrt{2\gamma/(\rho h)}$, which is known as the Taylor–Culick equation (27–29). In our experiments, the holes rapidly grow at $v_h \sim 1$ m/s until they coalesce with each other, which finally leads to the bursting of the spreading drop as shown in Figs. 1 *A–C* and 2 *C* and *D*.

Decrease in Contact Time. We measured the contact distance of a spreading drop, d, defined as the minimum distance between the drop center and the contact line on either the outer rim or a nucleated hole. Also, the contact time, $t_{\rm contact}$, was measured as the time interval between when a drop impacts and when the drop bounces off the substrate. For $U \leq U_c$, the contact time is approximate to the capillary contact time, $\tau = 2.3\sqrt{\rho R^3/\gamma}$, and the contact distance smoothly expands and retracts on the surface (Fig. 5*A*, open circles).

For $U > U_c$, the contact distance decreases discontinuously as several holes are nucleated (Fig. 5*A* and *SI Appendix*, section F). Through a series of hole coalescence, the drop bounces off from the surface quickly. Therefore, the contact time is significantly reduced as shown in Fig. 5*B*. The contact time decreases up to 70%, compared to its capillary contact time, τ (Fig. 5*C*). The upper and lower limits of $t_{\rm contact}/\tau$ are analytically evaluated by considering the aforementioned characteristics of hole nucleation (*SI Appendix*, section F).

Discussion

We showed that an impacting drop with high We ($100 <$ We $< 1{,}500$) generates intriguing shock-like patterns and undergoes vigorous fragmentation on hierarchical superhydrophobic surfaces. The shock-like waves are created in the presence of topographical bumps at the microscale. Then, the interference of the shock-like waves triggers hole nucleation and rupture, thereby breaking the drop into small satellite droplets. Such drop

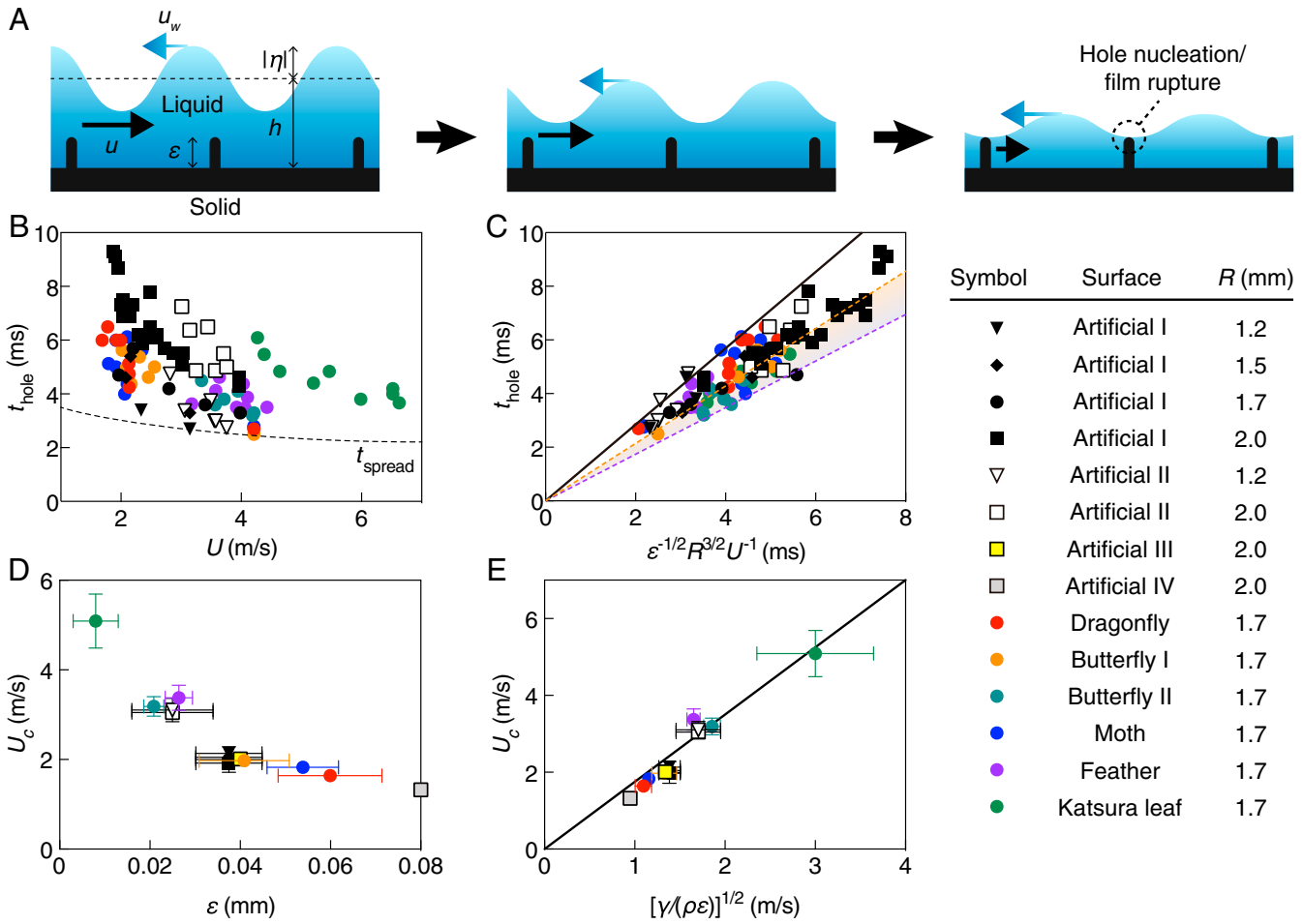

Fig. 4. (*A*) Schematic of shock-induced liquid–film rupture due to superhydrophobic microstructures. (*B*) Critical time for hole nucleation, t_{hole}, versus impact velocity, U. The dashed line represents the spreading time, which is defined as the time for the drop to reach its maximum radius. This spreading-time line is from a quadratic regression fit based on experimentally measured spreading times for $R = 1.7$ mm. (*C*) Experimental data in *B* replotted against our theoretical models. The solid line is obtained as the upper limit of t_{hole} (Eq. **3**), where the slope of the best-fitting line is 1.4. The dashed lines are determined by the lower limit of t_{hole} as in Eq. **2**, where the slopes of the best-fitting lines are $1.4[1 + a\sqrt{\rho/(\gamma k)}]^{-1/2}$. Here, the upper and lower dashed lines represent the maximum and minimum values among our surfaces, which correspond to butterfly I and bird feather, respectively. (*D*) Critical impact velocity, U_c, for different biological and artificial surfaces, which can be characterized by the height of microstructures, ϵ. (*E*) Experimental data in *D* replotted based on Eq. **4**, where the slope of the best-fitting line is 1.8.

dynamics result in a decrease in the contact time up to 70%, which may indicate potential advantages of various biological surfaces. Many biological surfaces are possibly contaminated by various impurities with different surface tensions. Then, the Marangoni stress induced by a spatial gradient in surface tension (30, 31) might affect the drop dynamics presented here. We tested the Marangoni effect by adding chemically coated impurities on the substrate. However, no significant change in the critical impact velocity was observed presumably due to the high Péclet number (*SI Appendix*, section G). Additionally, it is worth noting that our hole-nucleation model is different from previously studied hole-nucleation models based on energy balance (29, 32, 33). The previous models do not consider fluid flows and interfacial dynamics of a thin film, which play a crucial role in our rapidly spreading drop.

It is known that the exposure to rain can lower the body temperature of birds (34) and destabilize flying insects (35). The decrease in the drop-contact time limits the heat and momentum transfer onto organisms (4–6). Our quantitative measurements on various biological surfaces may unravel how birds lower hypothermia risks and how insects maintain flight stability as well as preserve regional heterothermy during rainfall. In addition, we observed that an impacting drop is shattered into smaller satellite droplets carrying plant pathogenic spores (*SI Appendix*, section H). This sheds light on an additional spore dispersal mechanism besides the recently discovered vortex-induced dispersal mechanism (36).

Table 1. Characteristic bump height ϵ and spacing s of experimentally used nonwettable surfaces

Surface	ϵ (μm)	s (μm)
Gannet feather	26 ± 3	316 ± 29
Dragonfly wing	60 ± 11	187 ± 27
Butterfly wing I (*P. marcellus*)	41 ± 10	89 ± 7
Butterfly wing II (*Hamadryas*)	21 ± 2	96 ± 4
Moth wing	54 ± 8	240 ± 18
Katsura leaf (21)	8 ± 5	25 ± 6
Artificial surface I	38 ± 7	445 ± 140
Artificial surface II	25 ± 9	266 ± 162
Artificial surface III	40	400
Artificial surface IV	80	400

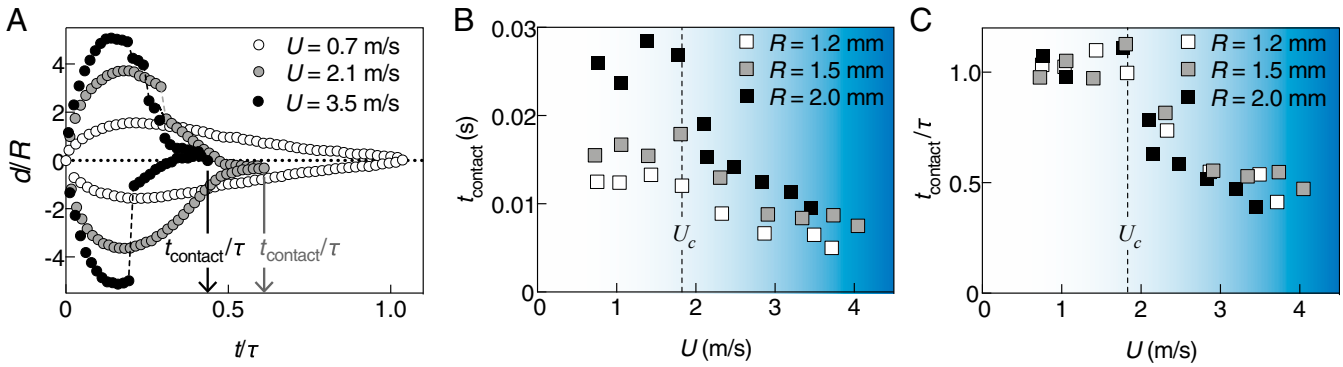

Fig. 5. (*A*) Temporal evolution of dimensionless contact distance d/R on artificial surface I with different impact velocities, U, for $R = 2$ mm. For $U < U_c$, an impacting drop symmetrically spreads and rebounds without forming a hole. For $U > U_c$, a rupturing hole starts forming during the drop-receding stage, which leads to the sudden decrease in d (the dashed lines in $U = 2.1$ m/s). For $U \gg U_c$, multiple holes nucleate earlier, thereby leading to the dramatic decrease in d and contact time. (*B*) Experimental contact time, $t_{contact}$, versus impact velocity, U, where the dashed line indicates the critical impact velocity, U_c. (*C*) Dimensionless contact time, $t_{contact}/\tau$, versus impact velocity, U, where the contact time of the impacting drop starts to decrease beyond the threshold impact velocity, U_c (dashed line).

Materials and Methods

Preparation of Biological Specimens. Bird feathers, insect wings, and katsura leaves were used because of their superhydrophobic property with hierarchical structures (17, 20, 21, 37, 38). For bird feathers, the carcass of northern gannet (*Morus bassanus*) was obtained from the Smithsonian Museum of Natural History. Insect samples were collected from the Cornell University Insect Collection, which had been gently killed in atmospheric conditions. Here, we used dragonfly (*Anax*), cecropia moth (*Hyalophora cecropia*), zebra swallowtail butterfly (*Protographium marcellus*), and cracker butterflies (*Hamadryas*). Katsura leaves (*Cercidiphyllum japonicum*) were obtained from near Tower Road, Ithaca, NY (42°26′52.7″N 76°28′26.1″W).

Preparation of Artificial Superhydrophobic Surfaces. We coated smooth glass substrates using a commercial nanoparticle spray (NeverWet; Rust-Oleum), which renders the glass substrate superhydrophobic with hierarchical structures (13). The spray coating consists of two different steps: step 1 and step 2. Step 1 and step 2 provide a layer of tiny particles creating rough physical morphology and a layer of hydrophobic adhesives with fewer particles, respectively. By selectively combining steps 1 and 2, we acquired two different superhydrophobic surfaces with varying roughness. Type I and type II artificial surfaces are created by applying either steps 1 and 2 or only step 2. Type III and type IV artificial surfaces are fabricated via a conventional soft lithography process, where we use polydimethylsiloxane (PDMS) as an elastomeric stamp. Square-shaped microbumps of 53 ± 4 μm × 54 ± 2 μm are regularly arrayed, where we change the height and the spacing of microbumps. Then, we treat the PDMS micropatterned surfaces with the step 2 spray to achieve superhydrophobic wettability. The spray-coated surfaces have the advancing and receding contact angles as $155 \pm 3°$ and $153 \pm 3°$, respectively.

Physical Property of Microbumps. A microscope was used to determine the physical property of microbumps on various surfaces. The microscopic images at different locations were taken, and the mean and SD values were calculated. The characteristic bump height, ϵ, and spacing, s, are listed in Table 1. The detailed methods of characterizing the surface morphology are described in *SI Appendix*, section I.

Drop Impact Experiments. A water drop is released at a certain height, falls under gravity, and then impacts a dry substrate. By choosing a syringe needle size and the drop-releasing height, the radius R and the impact velocity U of a water drop can be varied from 1.2 to 2.0 mm and from 0.7 to 6.6 m/s, respectively. The dynamics of an impacting drop are videotaped by two synchronized high-speed cameras (Fastcam SA-Z and Mini AX100) with a resolution of 1,024 × 672 pixels^2 at a frame rate of 5,000 to 20,000 s^{-1}.

Data Availability. All data and Matlab scripts are available on the Open Science Framework (DOI 10.17605/OSF.IO/6RD8K).

ACKNOWLEDGMENTS. We thank Hyunggon Park, Hope A. Gruszewski, and David G. Schmale III at Virginia Polytechnic Institute and State University for supplying and recording the drop dynamics on an infected wheat leaf. We also thank Kamel Fezza and Tao Sun at Argonne National Laboratory for helping us to set up and use the X-ray phase contrast imaging equipment. This work was supported by National Science Foundation (NSF) Grant CBET-1604424 and US Department of Agriculture Award 2018-67013-28063. This research used resources of the Advanced Photon Source, a US Department of Energy (DOE) Office of Science User Facility operated for the DOE Office of Science by Argonne National Laboratory under Contract DE-AC02-06CH11357. This work was performed in part at the Cornell NanoScale Facility, a National Nanotechnology Coordinated Infrastructure member supported by NSF Grant NNCI-1542081.

1. T.-G. Cha, J. W. Yi, M.-W. Moon, K.-R. Lee, H.-Y. Kim, Nanoscale patterning of microtextured surfaces to control superhydrophobic robustness. *Langmuir* **26**, 8319–8326 (2010).
2. Y. C. Jung, B. Bhushan, Wetting transition of water droplets on superhydrophobic patterned surfaces. *Scripta Mater.* **57**, 1057–1060 (2007).
3. D. Bartolo *et al.*, Bouncing or sticky droplets: Impalement transitions on superhydrophobic micropatterned surfaces. *Europhys. Lett.* **74**, 299–305 (2006).
4. J. C. Bird, R. Dhiman, H.-M. Kwon, K. K. Varanasi, Reducing the contact time of a bouncing drop. *Nature* **503**, 385–388 (2013).
5. S. Shiri, J. C. Bird, Heat exchange between a bouncing drop and a superhydrophobic substrate. *Proc. Natl. Acad. Sci. U.S.A.* **114**, 6930–6935 (2017).
6. D. Richard, C. Clanet, D. Quéré, Surface phenomena: Contact time of a bouncing drop. *Nature* **417**, 811 (2002).
7. R. Fürstner, W. Barthlott, C. Neinhuis, P. Walzel, Wetting and self-cleaning properties of artificial superhydrophobic surfaces. *Langmuir* **21**, 956–961 (2005).
8. J. Lv, Y. Song, L. Jiang, J. Wang, Bio-inspired strategies for anti-icing. *ACS Nano* **8**, 3152–3169 (2014).
9. X. Gao *et al.*, The dry-style antifogging properties of mosquito compound eyes and artificial analogues prepared by soft lithography. *Adv. Mater.* **19**, 2213–2217 (2007).
10. X. Yao *et al.*, Bioinspired ribbed nanoneedles with robust superhydrophobicity. *Adv. Funct. Mater.* **20**, 656–662 (2010).
11. S. Robson, G. R. Willmott, Asymmetries in the spread of drops impacting on hydrophobic micropillar arrays. *Soft Matter* **12**, 4853–4865 (2016).
12. Y. Liu *et al.*, Pancake bouncing on superhydrophobic surfaces. *Nat. Phys.* **10**, 515–519 (2014).
13. P. B. Weisensee, J. Tian, N. Miljkovic, W. P. King, Water droplet impact on elastic superhydrophobic surfaces. *Sci. Rep.* **6**, 30328 (2016).
14. E. S. Quintero, G. Riboux, J. M. Gordillo, Splashing of droplets impacting superhydrophobic substrates. *J. Fluid Mech.* **870**, 175–188 (2019).
15. E. Villermaux, B. Bossa, Single-drop fragmentation determines size distribution of raindrops. *Nat. Phys.* **5**, 697–702 (2009).
16. J. O. Laws, D. A. Parsons, The relation of raindrop-size to intensity. *Eos Trans. Am. Geophys. Union* **24**, 452–460 (1943).
17. E. Bormashenko, O. Gendelman, G. Whyman, Superhydrophobicity of lotus leaves versus birds wings: Different physical mechanisms leading to similar phenomena. *Langmuir* **28**, 14992–14997 (2012).
18. J. S. Roche, N. L. Grand, P. Brunet, L. Lebon, L. Limat, Pertubations on a liquid curtain near break-up: Wakes and free edges. *Phys. Fluid.* **18**, 082101 (2006).
19. I. Kim, S. Mandre, Marangoni elasticity of flowing soap films. *Phys. Rev. Fluids* **2**, 082001 (2017).
20. G. D. Bixler, B. Bhushan, Bioinspired rice leaf and butterfly wing surface structures combining shark skin and lotus effects. *Soft Matter* **8**, 11271–11284 (2012).

21. H. Kang, P. M. Graybill, S. Fleetwood, J. B. Boreyko, S. Jung, Seasonal changes in morphology govern wettability of katsura leaves. *PloS One* **13**, e0202900 (2018).
22. Y. Wang, L. Bourouiba, Drop impact on small surfaces: Thickness and velocity profiles of the expanding sheet in the air. *J. Fluid Mech.* **814**, 510–534 (2017).
23. C. Vernay, L. Ramos, C. Ligoure, Free radially expanding liquid sheet in air: Time- and space-resolved measurement of the thickness field. *J. Fluid Mech.* **764**, 428–444 (2015).
24. E. Villermaux, B. Bossa, Drop fragmentation on impact. *J. Fluid Mech.* **668**, 412–435 (2011).
25. A. Rozhkov, B. Prunet-Foch, M. Vignes-Adler, Dynamics of a liquid lamella resulting from the impact of a water drop on a small target. *Proc. R. Soc. Lond. Ser. A Math. Phys. Eng. Sci.* **460**, 2681–2704 (2004).
26. M. Pasandideh-Fard, Y. M. Qiao, S. Chandra, J. Mostaghimi, Capillary effects during droplet impact on a solid surface. *Phys. Fluid.* **8**, 650–659 (1996).
27. G. I. Taylor, The dynamics of thin sheets of fluid. III. Disintegration of fluid sheets. *Proc. R. Soc. Lond. Math. Phys. Sci.* **253**, 313–321 (1959).
28. F. E. C. Culick, Comments on a ruptured soap film. *J. Appl. Phys.* **31**, 1128–1129 (1960).
29. S. Kim, M.-W. Moon, H.-Y. Kim, Drop impact on super-wettability-contrast annular patterns. *J. Fluid Mech.* **730**, 328–342 (2013).
30. B. Néel, E. Villermaux, The spontaneous puncture of thick liquid films. *J. Fluid Mech.* **838**, 192–221 (2018).
31. S. Kim, J. Kim, H.-Y. Kim, Dewetting of liquid film via vapour-mediated Marangoni effect. *J. Fluid Mech.* **872**, 100–114 (2019).
32. R. Dhiman, S. Chandra, Rupture of thin films formed during droplet impact. *Proc. Math. Phys. Eng. Sci.* **466**, 1229–1245 (2009).
33. A. Sharma, E. Ruckenstein, Dewetting of solids by the formation of holes in macroscopic liquid films. *J. Colloid Interface Sci.* **133**, 358–368 (1989).
34. R. J. Kennedy, Direct effects of rain on birds: A review. *Br. Birds* **63**, 401–414 (1970).
35. A. K. Dickerson, P. G. Shankles, D. L. Hu, Raindrops push and splash flying insects. *Phys. Fluids* **26**, 027104 (2014).
36. S. Kim, H. Park, H. A. Gruszewski, D. G. Schmale, S. Jung, Vortex-induced dispersal of a plant pathogen by raindrop impact. *Proc. Natl. Acad. Sci. U.S.A.* **116**, 4917–4922 (2019).
37. C. Zhang, Z. Wu, X. Zhang, Y. Yue, J. Wang, Effect of feather elasticity of kingfisher wing on droplet impact dynamics. *JBE* **15**, 731–740 (2018).
38. K. Liu, L. Jiang, Bio-inspired design of multiscale structures for function integration. *Nano Today* **6**, 155–175 (2011).